Neuron
Article

A Biophysically Detailed Model of Neocortical Local Field Potentials Predicts the Critical Role of Active Membrane Currents

Michael W. Reimann,[1,4] Costas A. Anastassiou,[2,3,4,*] Rodrigo Perin,[1] Sean L. Hill,[1] Henry Markram,[1] and Christof Koch[2,3]
[1]Blue Brain Project, École Polytechnique Fédérale de Lausanne, Lausanne VD 1015, CH
[2]Division of Biology, California Institute of Technology, Pasadena, CA 91125, USA
[3]Allen Institute for Brain Science, Seattle, WA 98103, USA
[4]These authors contributed equally to this work
*Correspondence: costasa@alleninstitute.org
http://dx.doi.org/10.1016/j.neuron.2013.05.023

SUMMARY

Brain activity generates extracellular voltage fluctuations recorded as local field potentials (LFPs). It is known that the relevant microvariables, the ionic currents across membranes, jointly generate the macrovariables, the extracellular voltage, but neither the detailed biophysical knowledge nor the required computational power have been available to model these processes. We simulated the LFP in a model of the rodent neocortical column composed of >12,000 reconstructed, multicompartmental, and spiking cortical layer 4 and 5 pyramidal neurons and basket cells, including five million dendritic and somatic compartments with voltage- and ion-dependent currents, realistic connectivity, and probabilistic AMPA, NMDA, and GABA synapses. We found that, depending on a number of factors, the LFP reflects local and cross-layer processing. Active currents dominate the generation of LFPs, not synaptic ones. Spike-related currents impact the LFP not only at higher frequencies but below 50 Hz. This work calls for re-evaluating the genesis of LFPs.

INTRODUCTION

Extracellular voltage recordings (V_e), the voltage difference between a point in the extracellular space and a reference electrode, are the primary method of monitoring brain processing in vivo. Such recordings are high-pass filtered to isolate spiking. Slower V_e fluctuations (typically <300 Hz), referred to as local field potentials (LFPs), reflect the summed electric activity of neurons and associated glia and provide experimental access to the spatiotemporal activity of afferent, associational, and local operations (Buzsáki, 2004). The relationship between electric activity of nerve and (presumably) glia cells and the LFP has remained mysterious (for a review, see Buzsáki et al., 2012). LFPs have traditionally been viewed as a reflection of cooperative postsynaptic activity (Lindén et al., 2011; Mitzdorf, 1985). Yet, even when synaptic activity is blocked, neural populations can show emergent activity associated with large LFP deflections (Buzsaki and Traub, 1996; Buzsaki et al., 1988; Jefferys and Haas, 1982). What is clear is that nonsynaptic events, such as the spike afterpotential and intrinsic oscillatory membrane currents, can contribute to the recorded LFP (Anastassiou et al., 2010, 2011; Belluscio et al., 2012; Buzsáki et al., 2012; Buzsaki et al., 1988; Ray and Maunsell, 2011; Schomburg et al., 2012).

A major advantage of extracellular recording techniques is that, in contrast to other methods used to study network activity, the biophysics related to these measurements are well understood (Buzsáki et al., 2012). This has enabled the development of reliable and quantitative mathematical models to elucidate how transmembrane currents give rise to the recorded electric potential (Gold et al., 2006; Lindén et al., 2011; Pettersen et al., 2008; Schomburg et al., 2012). In particular, models emulating realistic morphology, physiology, and electric behavior, as well as connectivity, can provide insights into the origin of different kinds of extracellular signals because they allow precise control and access of all variables of interest. Here, we use a very large-scale model consisting of more than 12 thousand morphologically and functionally realistic neurons, simulated using more than five million spatial compartments and 35 million discrete synaptic and membrane currents, connected with each other based on rules that capture many aspects of measured connectivity (Hill et al., 2012; Perin et al., 2011). In particular, we account for the presence of neocortical (S1, hindlimb area) excitatory (layer 4, L4, and layer 5, L5, pyramidal neurons) and inhibitory (L4 and L5 basket cells) neurons. We investigate the impact of slow (approximately 1 Hz) external activity impinging on neurons and its effect on the resulting LFP signature.

Such rhythmic activity is relevant, for example, in the case of the most prominent of cortical processing, slow-wave activity (SWA, 0.1–1 Hz). Found in humans (Achermann and Borbély, 1997) and animals (Steriade et al., 1993a, 1993b, 1993c), SWA involves large areas of neocortex, along with various subcortical structures, that are synchronized into cyclical periods of global excitation followed by widespread silence. SWA is a defining characteristic of slow-wave, deep, or non-REM sleep but also occurs under anesthesia and in isolated cortical preparations. Neocortical cells discharge during the trough of the LFP and remain silent during the peak of the LFP recorded from deep layers of cortex. Active and silent periods of this slow oscillation are referred to as UP (high conductance) and DOWN (low

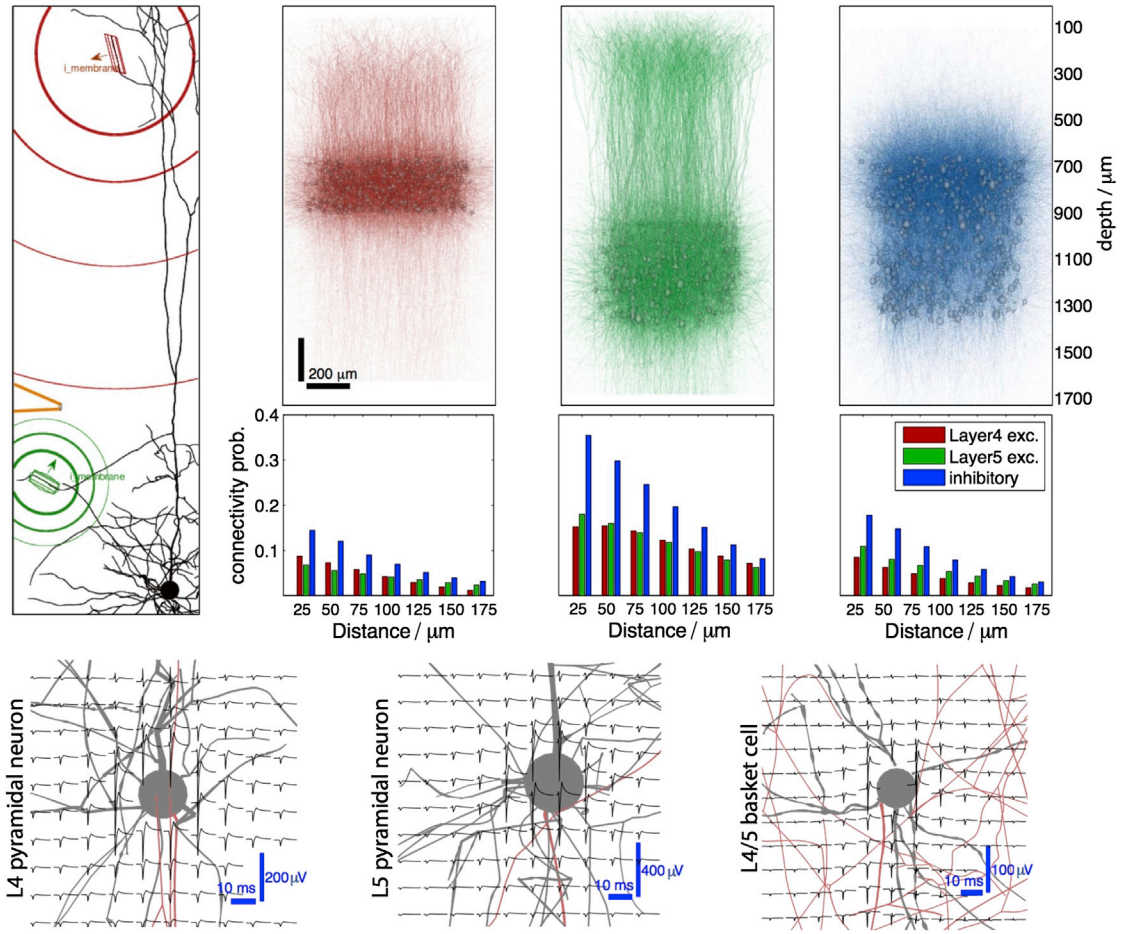

Figure 1. Intracellular and Extracellular Biophysics of Individual Neurons

First row: 5,471 morphologically reconstructed and interconnected L4 pyramids (red), 5,364 L5 pyramids (green), and 1,700 basket cells (blue). Circles indicate soma location, and the depth axis is shown on the right. Second row: connectivity probability (bars) as a function of distance to the soma and neural type (corresponding to the top row). For example, the probability that a basket cell is connected to a L4 pyramidal neuron located within 25 µm is approximately 0.16 (blue bar). Bottom row: extracellular action potentials around the cell body for the three neural types considered (L4 pyramids, L5 pyramids, L5 basket cell) induced by a brief (10 ms) intracellular somatic current pulse (gray: soma and dendrites; red: axons; see the Experimental Procedures). Left: transmembrane currents across all neural processes within a particular volume sum to make up the extracellular voltage fluctuations measured by an electrode (circles: isopotentials arising from two dendritic current sources). The line source approximation is used to calculate the extracellular contribution of transmembrane currents across each cylindrical compartment (see the Experimental Procedures).

See also Figure S1.

conductance) states. This robust neocortical oscillation coordinates various other rhythms, including spindles and delta waves (Steriade et al., 1993a, 1993b, 1993c) and faster activity (Mukovski et al., 2007).

Although we do not attempt to emulate the biophysical details of SWA involving a multitude of internal and external inputs, our large-scale, bottom-up biophysical model provides insights into the origin of the LFP signal, in the presence of active membrane conductances, realistic neural morphologies, and network connectivity patterns.

RESULTS

Based on hundreds of morphologically and functionally reconstructed neurons (Druckmann et al., 2007; Hay et al., 2011) (Figure S1 available online), the network model was built to capture many aspects of connectivity (Figure 1) (Hill et al., 2012; Oberlaender et al., 2012; Perin et al., 2011). Neural membrane processing of every compartment of every neuron is reflected in V_e by superposing membrane current contributions from each neural compartment using the line source approximation (Holt and Koch, 1999). That is, V_e at every location in extracellular space results from the linear summation of all membrane currents throughout the volume, scaled (to a first order inversely) by the distance to the current source (see the Experimental Procedures). In the present study, we focus on how the microscopic currents across each membrane sum to give rise to the macroscopic LFP signal and neglect any contributions that the LFP, in turn, might have on the voltage across each membrane (Anastassiou et al., 2010, 2011; Jefferys, 1995).

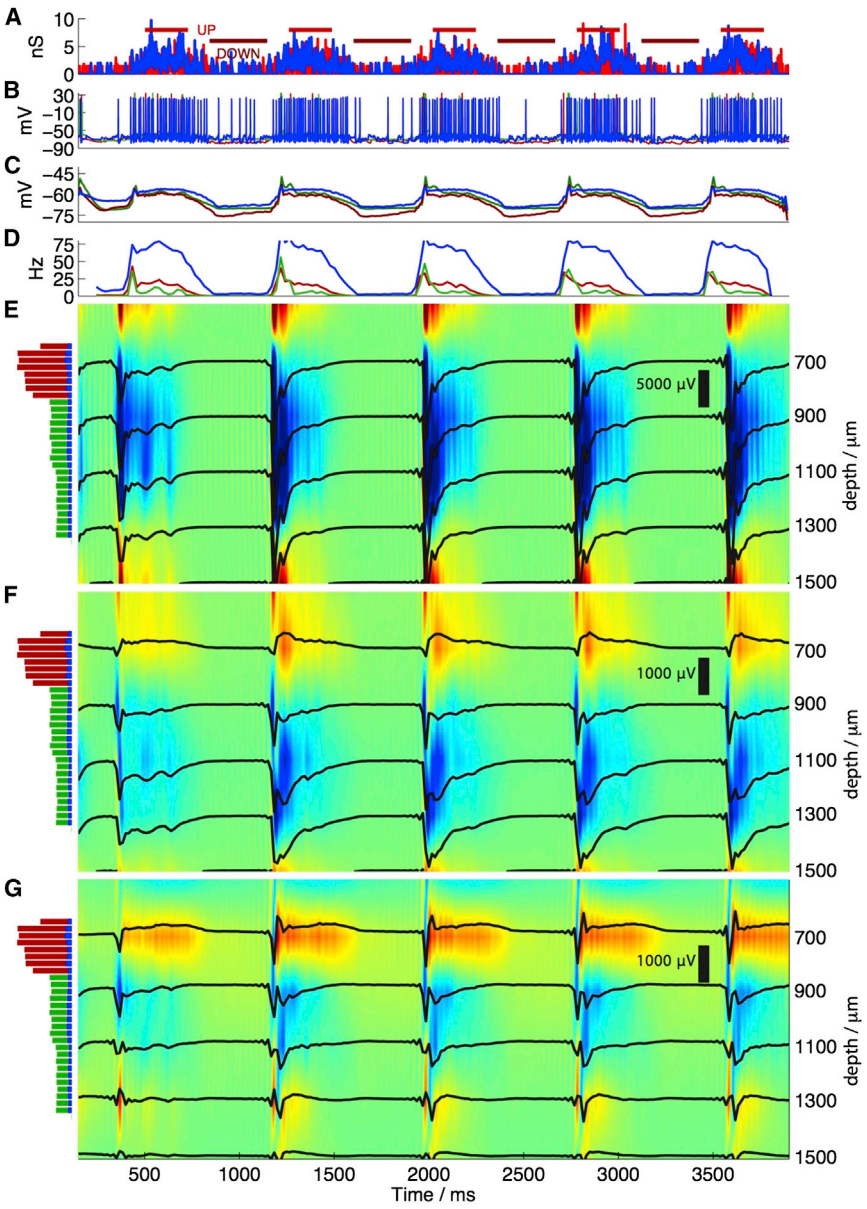

Figure 2. Simulated Network Activity

(A) External excitatory (red) and inhibitory (blue) synaptic input impinging on a L5 pyramid. In addition to more than 15 million synapses formed between the three types of neurons in our simulation, circa 750,000 additional synapses were placed on the pyramidal cells and activated by independent Poisson processes with a rate fluctuating at 1 Hz between 3 and 15 events per second for excitation and 0.3 and 1.5 events for inhibition. This input, impinging on L4 and L5 pyramids, drives network activity.

(B) Intracellular potential of three individual neurons (red: L4 pyramid; green: L5 pyramid; blue: L4 basket cell).

(C and D) Mean intracellular somatic potential (C) and spike frequency (D) (total number of spikes/total number of neurons/10 ms) as a function of time for all L4 (red) and L5 pyramids (green) and basket cells (blue).

(E–G) LFP and current source density (CSD) dynamics for postsynaptic excitatory and inhibitory currents (E) in the extracellular space, (F) impinging along morphologically realistic neurons with passive, or (G) with active membranes. LFP traces are plotted in solid black at different locations along the depth axis (vertical depth is 1 mm). CSD shown along the depth axis (blue: sink; red: source). (Left) Soma density of L4 (red) and L5 (green) pyramids and basket cells (blue) as a function of depth to indicate layering. (Right) Depth axis. Time axis, on the bottom, is identical for all panels.

See also Figures S1–S4 and Table S1.

Comparison between the extracellular action potential (EAP) traces elicited during simulated administration of brief (10 ms) intracellular somatic current injections (Figure 1, bottom row) and simulation as well as experimental observations (Gold et al., 2006) demonstrates that our single-neuron representations accurately reproduce the EAP waveform even though their reconstruction was optimized to reproduce intracellular rather than extracellular events (Hay et al., 2011). In fact, accurate simulation of the EAP waveform can be used as an additional (and often stricter) measure for the quality of the reconstruction of a neuron, especially for perisomatic compartments (Gold et al., 2007).

The prevailing view is that the LFP primarily reflects postsynaptic currents for frequencies lower than approximately 100–150 Hz (Nunez and Srinivasan, 2006), which stems from the recognition that extracellular currents from many individual compartments must overlap in time to induce a measurable signal, with such overlap primarily occurring for synaptic events (Elul, 1971; Logothetis and Wandell, 2004). This assumption, in turn, has motivated the study of LFPs using models that account for morphologically realistic but passive neurons with the statistics of postsynaptic currents and their spatial distribution emulating experimental observations. Yet, the presence of active conductances along the neural membrane is a highly nonlinear (either voltage- or ion-dependent) contributor of extracellular currents that cannot be accounted for via passive elements.

Figure 2 shows the outcome of a large-scale simulation in which slow (1 Hz) external excitatory (AMPA and NMDA) and inhibitory ($GABA_A$) synaptic activity impinged along both L4 and L5 pyramidal neurons (Figure 2A). For the active membrane simulation, this elicits spiking (Figure 2B), which, in turn, gives rise to local and global postsynaptic activity (Figures 2C and 2D). We define the depolarizing (hyperpolarizing) part of the external 1 Hz stimulation as UP (DOWN) state. The spike frequency (Figure 2D) of the different cell types considered in our simulations agrees with experimental observations in rodents during SWA (Fanselow

and Connors, 2010; Haider et al., 2006; Luczak et al., 2007, 2009; Sanchez-Vives and McCormick, 2000).

LFP Is Not Determined by Postsynaptic Currents Alone

To understand the different components contributing to the LFP, we considered three scenarios, each of which has identical spatiotemporal postsynaptic currents (PSC). We define the PSC to be the postsynaptic membrane current flowing at the synapse in response to the synaptic-associated conductance change, $I_{syn}(t) = g_{syn}(t)(V_m\text{-}V_{rev})$, with g_{syn} being the synaptic conductance, V_m is the membrane potential, and V_{rev} is the reversal potential (Koch, 1999). In the first scenario, we only consider the LFP caused by these currents from the roughly 15 million synapses (Figure 2E) by ignoring all nonsynaptic currents in the calculation of the LFP. Thus, the simulation reflects purely PSC activity and only accounts for the way synapses are arranged in space in the absence of neurons. In Figure 2F, we replay the identical PSC input along every neuron as in the full simulation (Figure 2G) but, in a more complex scenario than in Figure 2E, compute the LFP contributed by synapses plus the morphologically accurate but passive cables. Finally, the last scenario includes synapses as well as the morphology supplemented by all active membrane conductances (Figure 2G).

If we compute the LFP only from synaptic conductances (Figure 2E), excitatory input (mainly along the basal dendrites; Hill et al., 2012) on L4 and L5 pyramids gives rise to a negative LFP deflection extending across L4 and L5 at the onset of UP. The LFP negativity attenuates during the UP state due to synaptic depression (see the Experimental Procedures). During the DOWN state, synaptic activity is much reduced, resulting in an LFP close to zero.

How do morphological features of neurons impact the LFP? In Figure 2F, we replayed the pattern of PSC activation of Figure 2E, but this time we included morphologically detailed neurons (Figures 1 and S1) with passive membranes. In this setup, the LFP contributors are by definition limited to PSC and related passive "return" currents, i.e., currents induced along the neural membrane by impinging synaptic input due to charge conservation (Buzsáki et al., 2012). (Notably, the impact of return currents is absent in the simulation shown in Figure 2E.) All sodium, potassium, and calcium currents have been blocked. Oscillatory external inputs (Figure 2A) give rise to oscillatory intracellular depolarization (similar to Figure 2C). Yet, LFP features, such as the amplitude or the temporal width in the two layers, change drastically compared to Figure 2E. The presence of passive membranes markedly attenuates the amplitude and the temporal width of the LFP waveform (note the voltage scale bar in Figure 2E is 5-fold larger than in Figures 2F and 2G). This reduction is due to the impact of return currents of opposite sign that cancel out the extracellular impact of locally impinging synaptic input and low-pass filtering of passive membranes. In particular, the LFP waveform changes as a function of depth. This is especially true during the first 50–100 ms of UP.

Active Membrane Conductances of Within-Layer Pyramidal Neurons Crucially Shape the LFP

How do voltage- and ion-specific membrane conductances found in all of these neurons shape the LFP? The short answer is a lot, in particular, compared to the passive cable simulation (Figure 2F). The LFP amplitude in the active case (Figure 2G; mid L5 at approx. 1,100 μm cortical depth; mean amplitude: 0.8 mV (active) versus 1.3 mV (passive); mean half-wave width: 60 ms (active) versus 130 ms (passive); see also upcoming sections and Figure 4) is substantially attenuated. This is caused by the active conductances giving rise to a leakier membrane, especially at the onset and during UP, that, in turn, manifests itself in spatially extended extracellular multipoles of smaller amplitude (Figure S2). During DOWN, the difference between active and passive membrane leakiness is much attenuated because the membrane conductances in the state of near absence of synaptic input are almost identical (Figure S2). In general, adding return currents (via the inclusion of passive morphologies) and, in a subsequent step, increasing membrane leakiness (via the inclusion of active membrane conductances) leads to attenuation of the LFP amplitude and spatiotemporal width.

Given the linearity of the extracellular resistive milieu (Anastassiou et al., 2011; Logothetis et al., 2007 but also see Bédard et al., 2004), the LFP plotted in Figures 2E–2G is the sum of extracellular contributions from synapses and neurons distributed across two layers. In Figure 3, we segregate the LFP contribution of each neural type (top to bottom: L4 pyramids, L5 pyramids, L4/5 basket cells) for the case shown in Figure 2G. We observe that the LFP contributors within both layers are currents associated with L4 and L5 pyramids. More specifically, in L4, L4 pyramids contribute 46% ± 18% of the LFP (L5 pyramids contribution: 45% ± 18%), whereas in L5, L5 pyramids contribute 52% ± 20% (L4 pyramids contribution: 39% ± 18%). These results support the view that, under the conditions studied here, the LFP does not reflect only local population processing but also outer-layer activity (Figures 3A and 3B), especially in L4. The LFP in L5 is larger than in L4 due to the large size of L5 pyramidal neurons as well as the powerful synaptic drive they receive along their basal (mainly) and apical dendrites (Figure 2G). This elicits membrane currents along the whole depth axis (Figure 3B) so that, while perisomatic compartments still contribute mostly to the LFP, the apical dendrites of these neurons also contribute to the LFP in L4, especially during the transition from DOWN to UP, i.e., during the highly synchronous barrage of excitation impinging on L5 pyramidal neurons.

Comparatively, L4/5 basket cells, making up only 13% of all cells with their temporally narrow EAPs (Figure 1, bottom) (Schomburg et al., 2012) and fairly symmetric and localized dendritic arbors, contribute very little to the LFP in either layers (basket cell contribution is 9% ± 2% in L4 and 9% ± 6% in L5; Figure 3C). The negligible contribution of L4/5 basket cells to the LFP is in stark contrast to their particularly high level of activity (their spiking rate reaches up to 75 Hz during UP, Figure 2D), compared to L4 and L5 pyramidal neurons in our simulations.

The simulated LFP contributions of L4 and L5 pyramids capture a common experimental observation: the positive LFP deflections in the perisomatic region and the negative LFP deflection along basal and apical dendrites during somatic depolarization periods (especially at UP onset; see also Figure 4) can be attributed to the location of excitatory and inhibitory conductances along the elongated morphology of neurons in combination with the presence of return currents (Buzsáki et al., 2012).

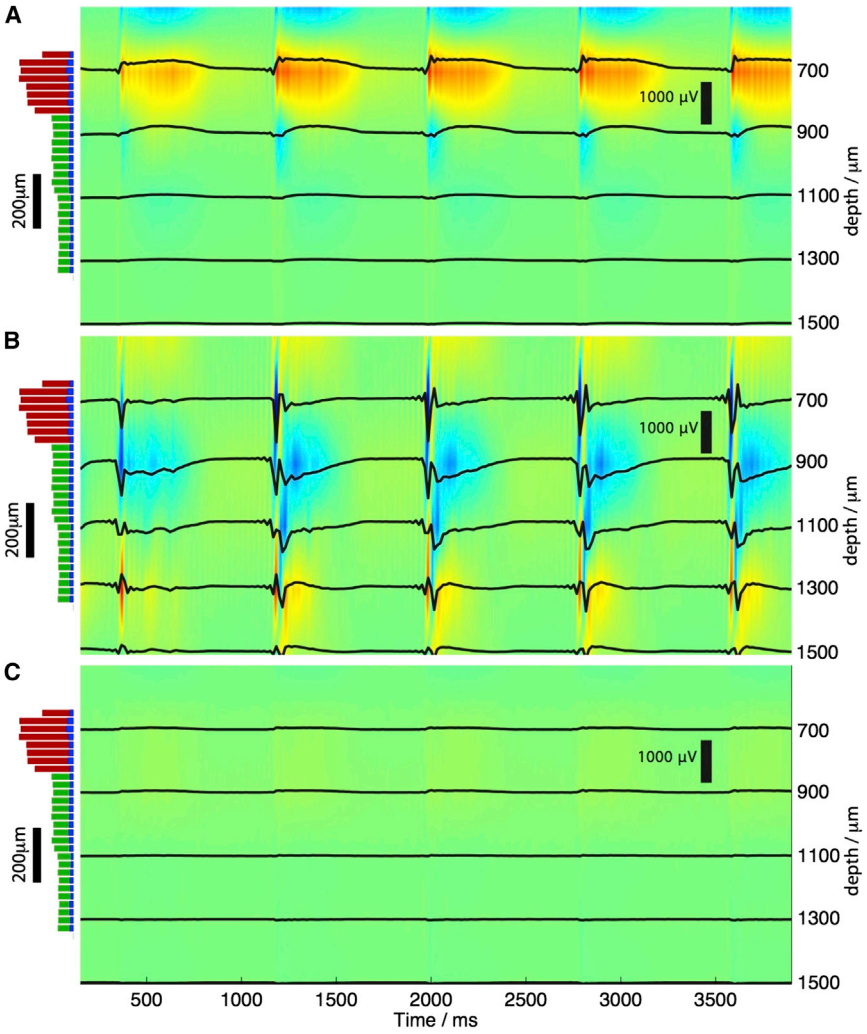

Figure 3. LFP and CSD Contribution of Individual Cell Populations

(A–C) The LFP and CSD contribution of (A) L4 pyramidal neurons, (B) L5 pyramidal neurons, and (C) L4/5 basket cells as a function of depth for the active conductance simulation shown in Figure 2G. CSD is shown along the depth axis (blue: sink; red: source).

See also Figures S2 and S3 and Table S1.

Active Membrane Conductances Alter LFP and CSD Amplitude, Spatial Width, and Constellation

To quantify differences in the spatial extent of the LFP between the passive (Figure 2F) and active membrane (Figure 2G) simulations, we fit the sum of two, spatially displaced, Gaussian functions (independent variable: location along the depth axis) of opposite sign to the mean LFP depth profile during UP (Figures 4A–4C) and determined the amplitude, peak location, and the LFP length scale (described by the half width of each of the Gaussians). We found that the amplitude changes by approx. 50%–300%, the location by 100–300 µm, and the spatial width by 30%–40% (values determined 50 ms after onset of UP; Figure 4D). Differences between active and passive are even greater during the first 50 ms of UP states (Figure 4A), but we chose to compare LFP depth profiles after synaptic activity had propagated throughout the network. Thus, in both layers, the presence of spiking and spike-related currents drastically alters LFP depth characteristics (amplitude, spatial, and temporal constellation), with differences being more pronounced in L5 especially during the first 100 ms of UP (Figure 4A). On the other hand, in L4, the LFP traces for the active and passive simulation are more similar, suggesting that the LFP there reflects not only active membrane processing but also synaptic and passive processes.

Current source density (CSD) analysis estimates the negative second-order spatial derivative of the LFP along the depth axis of the recordings. Per definition, the CSD represents the volume density of the net current entering or leaving the extracellular space (Nicholson and Freeman, 1975) and is used as a measure of synaptic input eliciting so-called current sinks (for excitatory inputs) and sources (for inhibitory inputs). In contrast to the LFP that is a distance-weighted superposition of currents within a small volume, the CSD crucially depends on local events along the depth axis. Thus, it is a better measure for processes occurring along the extent of L4 and L5 pyramids.

We calculated the one-dimensional CSD along the 1 mm depth axis covering L4 and L5 (Figures 2E–2G and 3; sinks are in blue, and sources are in red). In the presence of active membrane conductances, sodium influx and potassium efflux associated with spiking gives rise to sinks and sources, respectively, in the vicinity of cell bodies. The oscillatory pattern of impinging synaptic inputs gives rise to a temporally oscillatory CSD of the same frequency as well as an intricate spatial structure of the waxing and waning of two sources (one in each layer) and one sink (in L5) with a length scale of approximately 250 µm. The aforementioned LFP differences (amplitude, spatial, and temporal variance) are also reflected in the CSD characteristics with passive membranes resulting in temporally wider CSD and differential sink-source constellation along the depth axis (Figures 2F and 2G). Notably, a current source is present in deep L5 for active membranes at UP onset (Figure 2G, red areas) that vanishes in the passive case. More generally, passive membranes exaggerated the strength and spatial reach of the induced multipoles along pyramidal neurons (Figures 2F, 2G, and 4A–4D). Examination of the CSD contribution of the individual neural types (Figures 3 and S3) revealed that the presence of active versus passive membranes altered the overall sink-source constellation and individual neural type contributions. Yet, for the stimulation scenarios examined in this paper, the contribution of L5

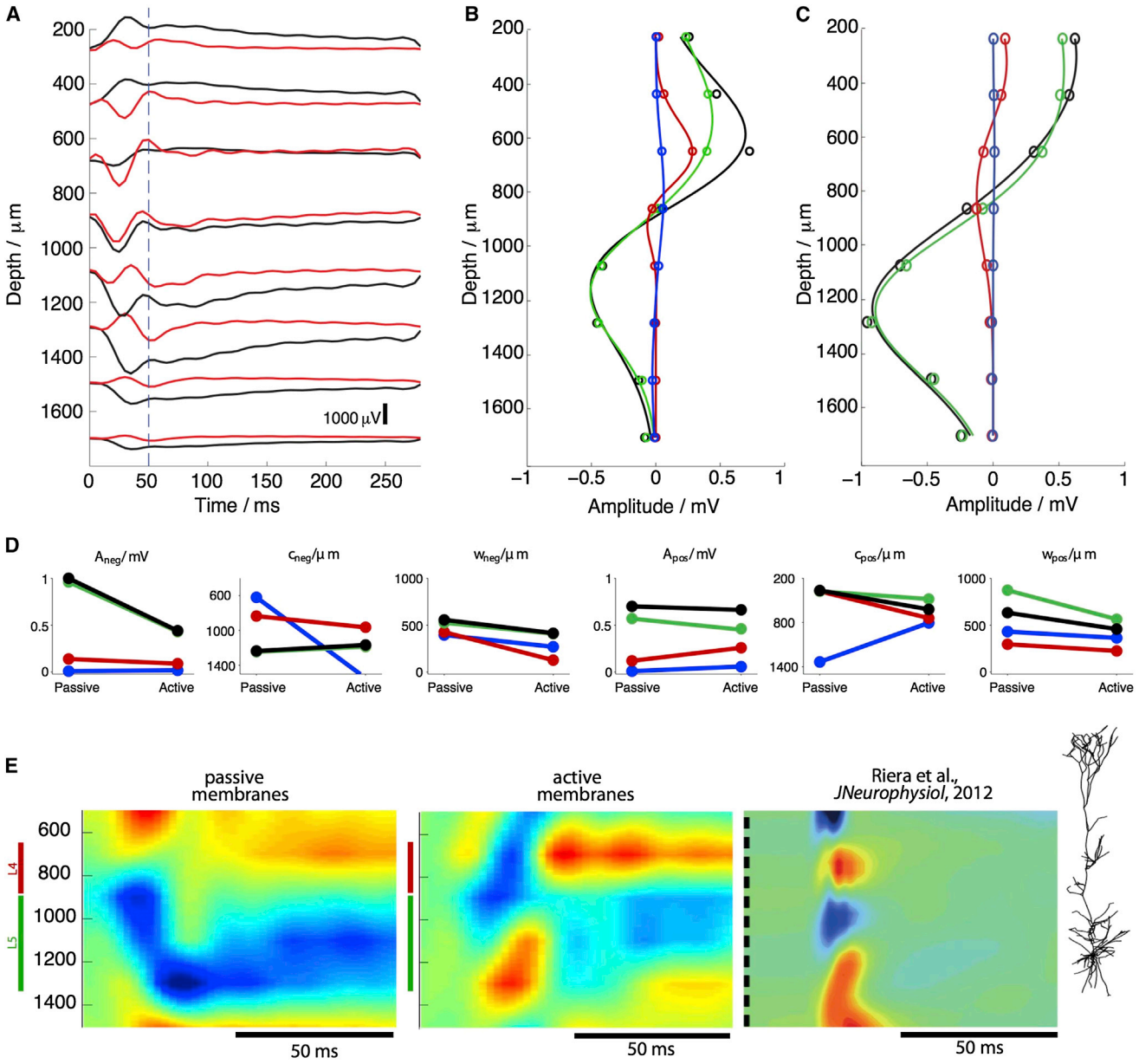

Figure 4. Comparison of the LFP Depth Profiles between Active and Passive Membranes

(A) Average LFP trace as a function of cortical depth during the mean UP state (mean calculated over the five UP states in Figure 2) for passive (black; simulation in Figure 2F) and active (red; simulation in Figure 2G) membranes. The blue line indicates the 50 ms instant on which the analyses shown in (B)–(D) are based.

(B) The contribution of all neurons (black), layer 4 (red) and layer 5 pyramids (green), or L4/5 basket cells (blue) as a function of depth (circles: simulation results; line: best fit with double Gaussian function) in the center of the neural population for active membranes.

(C) Same as (B) but for passive membranes.

(D) Amplitude of the negativity (A_{neg}) and positivity (A_{pos}), location (c_{neg} and c_{pos}, respectively), and the half-width of the LFP extrema (w_{neg} and w_{pos}, respectively) of the double Gaussian fits for active (red) and passive (black) membranes (see also Table S1). Color coding as in (B) and (C).

(E) Comparison of network simulations with experimental data. Left: mean CSD of simulation (time zero: UP onset; Figure 4A) with purely passive membrane conductances (simulation shown in Figure 2F). Middle: mean CSD of simulation, including active membrane conductances (simulation shown in Figure 2G). Right: grand average (n = 13 rats) CSD from recordings in rat somatosensory barrel cortex during single-whisker deflections (Riera et al., 2012). The dashed vertical line on the left indicates the time instant for the whisker deflections. The position of L4 (red) and L5 (green) is indicated by the bars on the left and depth (in µm). The right panel is partly adopted from Riera et al. (2012) and aligned to the simulation CSDs so as to show the same depth coordinates (a L5 pyramid is shown on the right for comparison).

See also Figure S2.

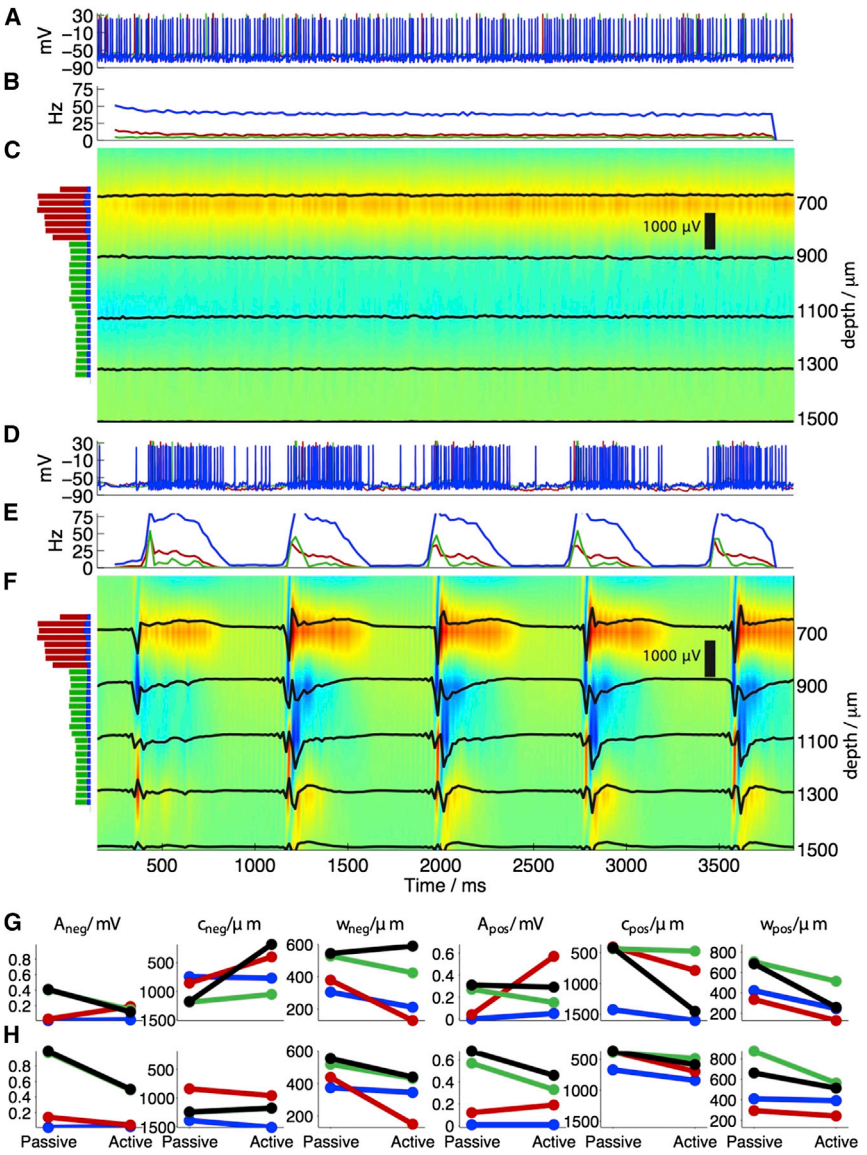

Figure 5. Altered Synaptic Input Correlation Driving L4 and L5 Pyramidal Neurons

(A–H) Two cases with altered synaptic input correlation driving L4 and L5 pyramidal neurons (compared to "control" in Figure 2): one with decreased ("decorrelated," A–C and G) and one with increased input correlation ("supersynchronized," D–F and H). (A) Intracellular potential of three individual neurons (red: L4 pyramid; green: L5 pyramid; blue: L4 basket cell). (B) Spiking frequency as a function of time for all L4 (red) and L5 pyramids (green) and basket cells (blue). (C) LFP and CSD dynamics resulting from decorrelated input impinging along morphologically realistic neurons with active membranes. (D–F) Same as (A)–(C), respectively, for the "supersynchronized" case. (G and H) Amplitude of the negativity (A_{neg}) and positivity (A_{pos}), location (c_{neg} and c_{pos}, respectively), and the half-width of the LFP extrema (w_{neg} and w_{pos}, respectively) of the double Gaussian fits for active (red) and passive (black) membranes (see also Table S1) for (G) the "uncorrelated" and (H) "supersynchronized" cases (same color-coding as in Figure 4D).
See also Figures S2 and S4.

pyramids continues to dominate also in terms of CSD (Figures 3B and S3B).

Experimentally Measured Sink-Source Constellation Replicated by Simulations

Which CSD, passive (Figure 2F) or active (Figure 2G), is closer to CSDs obtained in vivo? Answering this question involves comparing CSDs during various brain states that can differ greatly. Riera et al. (2012) recently conducted detailed experiments in rat somatosensory barrel cortex and measured the CSD along the depth axis of barrel cortex during single whisker deflections. In Figure 4E, we plot the CSD for (left to right) the passive simulation (mean of the data shown in Figure 2F aligned at UP onset; Figure 4A), the active membrane simulation (mean of the data shown in Figure 2F aligned at UP onset; Figure 4A) and the grand average measured by Riera and colleagues (their Figure 3). We observe how at UP onset and during the first 10–20 ms, sink-source constellation in L4 and L5 is similar to in vivo experiments. Subsequently, following synaptic depression in L5 attributed to particularly synchronous spiking, the two scenarios differ markedly for the next 10–20 ms with the sink-source constellation inverting. Finally, after equilibration of synaptic weights in L4, the active membrane simulation becomes almost identical to experiments. Notably, the resemblance between simulated and measured CSDs is greatly diminished when assuming identical synaptic input but passive membranes (Figure 4E, left), with the sink in L5 being exaggerated and the source almost absent from L4. (The resemblance becomes even poorer when comparing the experimental CSD to the PSC case shown in Figure 2E.) Although this comparison needs to be extended across multiple brain states, it suggests that active membrane conductances have a powerful influence on the CSD.

Synaptic Input Correlation Differentially Reflected in Sink-Source Features, Depending on Membrane Conductances

How do LFP characteristics change with input statistics? Synaptic input correlation crucially impacts the spatial extent of the LFP (Lindén et al., 2011; Pettersen et al., 2008; Schomburg et al., 2012). We performed simulations in which we either eliminated ("uncorrelated" case; Figures 5A–5C) or further enhanced ("supersynchronized" case; Figures 5D–5F) the temporal

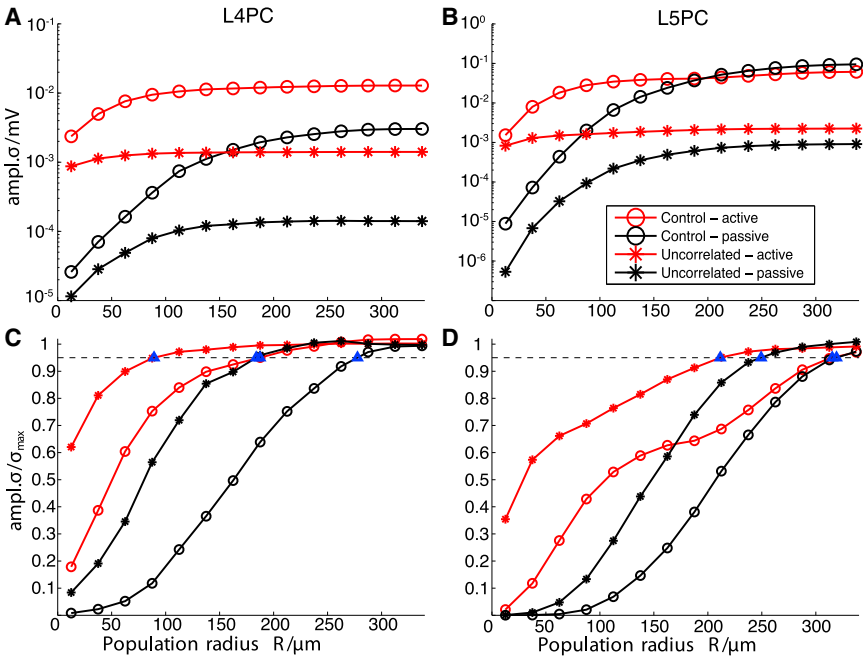

Figure 6. LFP Contribution as a Function of Lateral Distance

(A–D) (Left) L4 and (right) L5 pyramidal neuron population was separated in concentric cylinders of radii R. (A and B) Cumulative contribution of each additional cylinder to the LFP amplitude measured in the center of each population (red: active membranes; black: passive; circle: control input; star: uncorrelated input) with σ defined as the SD of the LFP signal during four UP states. (Notably, σ differs from the LFP amplitude definition in Figures 4 and 5.) (C and D) Rescaled version of panels (A) and (B) with the LFP amplitude expressed as fraction of the asymptotically reached amplitude (95% of the maximum value). The vertical distance R^*, where the LFP amplitude equals 95% of the asymptotically reached LFP amplitude is designated by blue triangles.

correlation of impinging synaptic input compared to the simulations shown in Figure 2G (termed the "control" case). Importantly, the "uncorrelated" and "supersynchronized" simulations have an identical number of PSCs impinging at the same locations as the "control" simulation. Only their timing is shifted, reflecting a decrease or an increase in input correlation (see the Experimental Procedures; Figure S4). As synaptic drive becomes more correlated, the LFP amplitude increases (Figure 5C versus 5F). To quantify such differences, we use the same method as introduced in Figure 4 and report amplitude, location, and spatial width of the two spatially displaced Gaussian functions 50 ms after UP onset (Figures 5G and 5H; see also Table S1).

For example, the amplitude of the LFP negativity (fit by a Gaussian), A_{neg}, increases with input correlation: 0.12 mV (uncorrelated) versus 0.36 mV (control) versus 0.50 mV (supersynchronized) (Table S1). We see that the extent of the amplitude decrease for passive versus active membranes depends on cell type, with the greatest effect observed for L5 pyramids due to their size and strong synaptic drive.

As witnessed by Figures 2, 4, and 5, identical synaptic input causes larger LFP amplitudes for passive than for active membranes for almost all input correlation scenarios considered. For example, for the "control" simulation, identical synaptic activity gave rise to A_{neg} = 0.99 mV and A_{pos} = 0.68 mV for passive membranes versus A_{neg} = 0.50 mV and A_{pos} = 0.46 mV for active membranes (Table S1). Increased input correlation generally resulted in an increase in the length scale of the LFP, both for active and passive membranes, with L5 pyramids most strongly affected (compare spatial width *w* in Figure 5G versus 5H; Table S1). Again, passive membrane simulations have a larger spatial extent than active ones (manifested in the negative slope in almost all *w*-related panels in Figures 4D, 5G, and 5H).

So far our analyses have focused on the LFP and CSD features along the cortical depth axis. Assuming extracellular recording sites are situated along the center of the cortical disk, how do LFP characteristics change along the radial axis, that is, tangential to the cortical sheet? In Figure 6, we segmented the population into concentric cylinders of radii R and calculated the LFP amplitude contributed in the center of L4 (left column) and L5 (right column) as a function of R. Accounting only for the V_e contribution of pyramidal neurons within a certain layer, we adopted the approach introduced in Lindén et al. (2011) (their Figure 5) to calculate the LFP contribution for the uncorrelated (stars) and control (circles) case for active (red) and passive (black) membrane conductances. Briefly, we defined the LFP amplitude σ as the SD of the LFP signal (Figures 6A and 6B) and the LFP saturation distance R^* (Figures 6C and 6D; blue triangles) as the radius at which the LFP amplitude reaches 95% of its maximum value with neurons located farther from R^* having a small contribution to the LFP signal. (Importantly, LFP amplitude σ is not the same as *A* reported in Figures 4D, 5G, and 5H). Similar to Lindén et al. (2011), we found that increasing input correlation increased R^*. Yet, as for the analyses along the cortical depth axis, the presence of active membranes reduced R^* (active versus passive in L4: uncorrelated, 89 versus 184 μm; control, 187 versus 278 μm; L5: uncorrelated, 212 versus 249 μm; control, 315 versus 319 μm), especially in L4. Interestingly, for uncorrelated input in L5 and passive membranes, R^* from our simulations (249 μm) is in agreement with the value reported by Lindén et al. (2011) (approximately 200 μm; their Figure 5c).

LFP Composition Is Transient and State Dependent

So far, we focused on the LFP contribution of different cell types. Given the critical role of active membranes, which channels impact the LFP most and under which conditions? To address this question, we calculate the LFP contribution of synaptic input as well as the specific ions sodium (Na), potassium (K), and calcium (Ca) of the different cell types separately and show them for

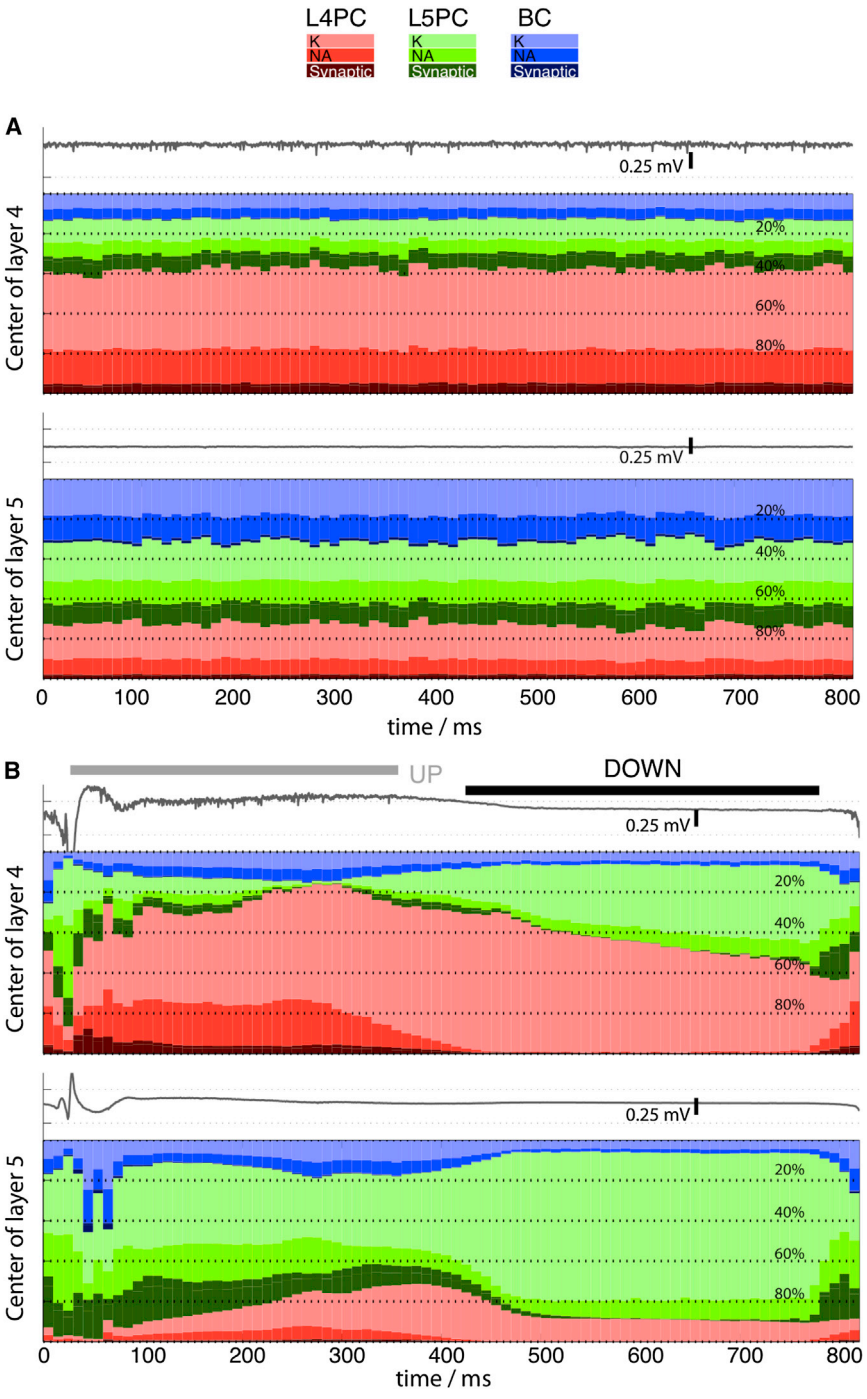

Figure 7. Ionic Contributions to the LFP

(A and B) Three types of LFP contributions are considered: excitatory and inhibitory postsynaptic currents (synaptic) as well as Na-related (NA) and K-related (K) membrane currents as measured in the center of L4 (top) and L5 (bottom). Ca-related currents were also calculated, but their contribution was small (less than 2.5%) and is neglected. Temporal binning is 10 ms. To calculate the contribution at the time bin of interest, the synaptic and active charge contribution (return currents are not included) of a particular neural population is weighted by the distance. In a second step, we normalized the contribution to the LFP amplitude generated by the population as shown in Figure 3. (The reason for the second step is to ensure that the sum of Na, K, and synaptic contributions of a cell type population equals the total contribution of that population to the overall LFP.) For example, the contribution of Na-related conductances of L5 pyramids is the total charge moved across the membrane via active Na-conductances during a particular time bin weighted by the inverse of the distance to the electrode. Then we divide the charge contributed by Na-related conductances by the total charge contributed by all conductances of L5 pyramids. The contribution of the three cell types is considered separately: L4 pyramidal neurons (red), L5 pyramidal neurons (green), and basket cells (blue). The data are presented in form of relative (stacked) percentual contributions. (A) The results for the "uncorrelated" simulation (Figures 5A–5C). (B) The results for the "control" simulation (Figure 2F). Notably, inhibitory postsynaptic currents contribute approximately 10% of the total synaptic contribution, i.e., excitatory input dominates the synaptic contribution.

two cases, "uncorrelated" and "control" (Figure 7). (Performing the same analyses for the "supersynchronized" case yields very similar results to "control".) Specifically, we define the normalized portion of the LFP signal attributed to the current passing from a particular conductance integrated over the time bin (resulting in charge) as LFP contribution. We calculated the LFP contribution of specific conductances in two locations, the center of L4 and L5. For the "uncorrelated" case (Figure 7A), synaptic excitatory and inhibitory currents contribute under 15%–20% to the LFP. Fast sodium currents, especially from local pyramidal neurons, contribute about 30%, with the rest of the contribution stemming from slower potassium currents. Interestingly, whereas L5 pyramids expectedly (due to the presence of thick apical dendrites) contribute to the LFP recorded in L4, L4 pyramids also contribute to the LFP recorded in L5, mainly via K-related currents. The main contribution of L4/5 basket cells is in L5, where sodium and potassium currents constitute about 30% of the total current, yet it needs to be pointed out that the LFP amplitude for uncorrelated input is small (see Figure 5G and traces in Figure 7).

How do these contributions change with input correlation? For the "control" case (Figure 7B), we observe how spiking Na and K currents from L5 pyramids dominate the LFP 20–40 ms from UP onset, both in L4 and L5. In fact, in L4, the LFP contribution from postsynaptic input impinging on L5 pyramids is larger

than the LFP contribution of postsynaptic input impinging along L4 pyramids. Concurrently, there is a strong activation of Na- and K-related currents through spiking of L5 pyramids that prominently contribute to the LFP in L4. It is after the initial transient of 40 ms that synapses of L5 pyramids depress at which point Na- and K-related currents of L4 pyramids begin dominating (approx. 60%–80%) the LFP signal in L4. In L5, within-layer pyramids dominate the LFP throughout the UP-DOWN cycle with two main differences to L4 activity: first, synaptic currents contribute more (approx. 15%–20%) than in any other case during UP, and second, L4/5 basket cells have a significant (even if short-lived) impact on the LFP 50 to 70 ms from UP onset (approx. 30%–40%), where dense local connectivity (Figure 1) and the massive bolus of postsynaptic activity induces high spiking rates (Figure 2). Finally, we found IPSCs to contribute approximately 10% of the total (excitatory and inhibitory) synaptic contribution, i.e., under the conditions studied here excitatory input dominates the synaptic contribution.

Frequency and Distance Scaling of LFPs Is Determined by Active Membrane Currents

Temporal frequency (“1/f”) and distance (“1/r”) scaling of LFP signals can reveal aspects of neural processing (Bédard et al., 2006; Katzner et al., 2009; Miller et al., 2009; Milstein et al., 2009; Pritchard, 1992; Rasch et al., 2009). Which sort of scaling do our simulations exhibit? Using the V_e traces recorded in depths ranging from 500 to 1,700 μm (representative V_e traces shown in Figure 8A; blue: PSC only, black: passive membranes, red: active membranes), we initially calculated the power spectral density (PSD) P (“control” simulations in Figure 8B; line: mean, shaded area: SD). We calculate the best fit (see Table S2) to $P(f) \propto 1/f^{\alpha}$ with f being the frequency and α the scaling exponent for two bandwidths: <40 Hz (Figure 8C, bottom) and 40–1,000 Hz (Figure 8C, top). α is consistently smaller across all cases of input correlation for low frequencies compared to high ones (circles: mean; error bars: SEM), with the differences in α between all cases being small for <40 Hz (Table S3). For 40–1,000 Hz, α is similar between PSC and passive membrane simulations, while substantially reduced for active membranes (Table S3). For example, for the “control” simulation with active membranes, $\alpha = 2.0 \pm 0.4$, whereas for passive membranes, $\alpha = 3.7 \pm 0.1$. (For <40 Hz, for the “control” simulation, $\alpha = 1.0 \pm 0.2$ and 0.9 ± 0.1, respectively.) Notably, experimental recordings exhibit α close to two (Miller et al., 2009; Milstein et al., 2009), with α smaller at lower frequencies (Miller et al., 2009). We conclude that α is crucially shaped not only by postsynaptic currents but also by membrane characteristics in the 40–1,000 Hz range.

How do individual neurons and the associated microvariables give rise to such frequency-scaling evident in the macrovariables, i.e., the LFP? To address this question, we defined a single-cell frequency scaling exponent for all L5 pyramidal neurons (the population with the strongest LFP contribution), where $P(f) \propto 1/f^{\beta}$, and calculated the mean V_e of all 5,364 L5 pyramidal neurons at three different locations relative to the soma (Figures 8D and 8E shows the “control” simulation). The PSD as well as its frequency scaling differs substantially depending on whether only PSC, passive cable structures, or active membranes contribute to the LFP. PSC and passive membranes consistently give rise to steeper scaling and larger β (approx. 2.5–3; Figures 8E and 8F; Table S4) for all simulations, whereas for active membranes β is smaller (approx. 1–2; Table S4). The PSD decreases drastically as a function of frequency for passive membranes and decreases much less so for active membranes (Figure 8E). More surprisingly, differences in PSD as well as frequency-scaling for active versus passive membranes persist for frequencies <100 Hz (Figure 8E). This suggests that spiking and spike-related currents contribute to low LFP bandwidths traditionally considered to reflect purely synaptic activity, an observation that agrees with experiments demonstrating LFPs generated via non-synaptic events (Anastassiou et al., 2010; Buzsáki et al., 2012; Chrobak et al., 2000).

The spatial extent of LFPs changes substantially between cases (Figures 4 and 5). We analyzed the LFP contribution of L5 pyramids to three bandwidths (<50, 50–100, and 800–1,000 Hz; Figure 8G), as a function of distance r between the soma and the electrode, i.e., $P(r) \propto 1/r^{\gamma}$, with $P(r)$ as the distance-dependent PSD in a particular bandwidth, and γ is the distance-dependent exponent (Figures 8G–8I). In agreement with Lindén et al. (2011), Pettersen et al. (2008), and Schomburg et al. (2012), we found that for passive membranes, $\gamma < 2$ for $r < 100$ μm, increasing to $\gamma \approx 3$ for larger distances (Figure 8I). This observation was robust for all bandwidths and input correlations we examined. In the presence of active membrane conductances, PSD distance scaling changed substantially closer than 100 μm (Figures 8H and 8I), with $\gamma \approx 3$ for all distances and input correlation scenarios. This suggests that active membrane conductances in L5 pyramids consistently generate extracellular multipoles (Pettersen et al., 2008; Riera et al., 2012). Notably, PSC simulations, consistent with the point-like nature of synaptic input, give rise to monopoles close to the recording electrode and dipoles when measured farther away. As illustrated in Figure 8H (and already suggested by Figures 8B and 8E), PSD not only differs in the higher bandwidths, where spiking currents dominate, but, surprisingly, also below 50 Hz. Given the identical synaptic activity between PSC, passive and active membrane simulations, these differences are attributed to the active membrane properties that not only give rise to a leakier membrane but fundamentally alter the sink-source constellation.

DISCUSSION

We use a large-scale computational model with more than five million compartments to study the extracellular signature of active brain tissue, the LFP. The model accounts for biophysically characterized and morphologically reconstructed neurons interconnected based on rules supported by experimental data. Traditionally, the LFP has been assumed to reflect postsynaptic currents and associated passive return currents, with the final extracellular field mainly shaped by neural morphology and synaptic input. Our simulations challenge this picture. With identical synaptic input waxing and waning at 1 Hz, active membrane conductances cause markedly different LFP signatures than passive cable structures or only postsynaptic activity without any passive or active membranes. These differences are not merely due to the amount of current flowing through the

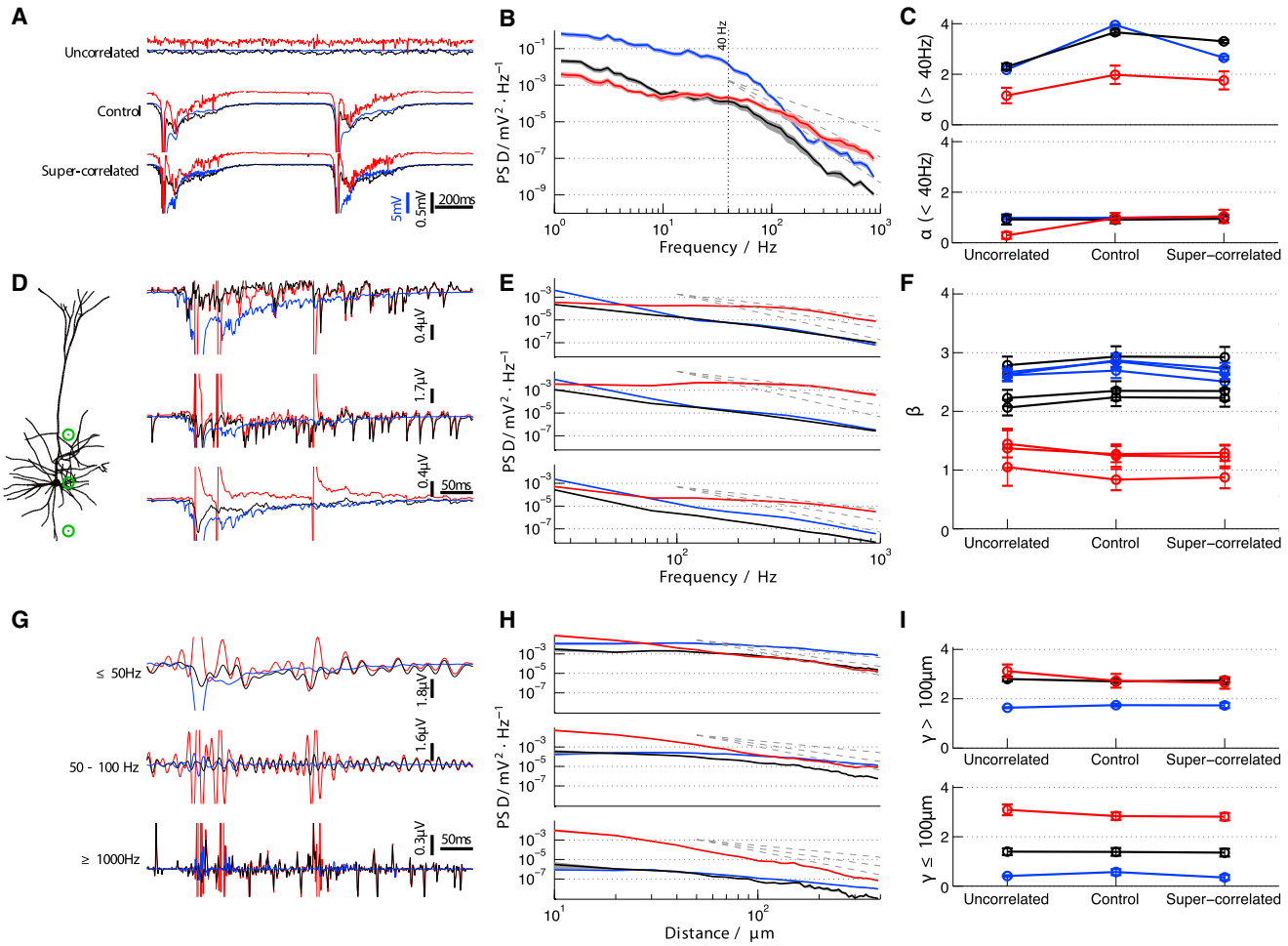

Figure 8. Frequency and Distance Scaling of the LFP

(A) A 2-s-long period of the V_e recording conducted in the middle of L5 for (top to bottom) uncorrelated, control, and supercorrelated inputs (blue: only PSC contribute toward the LFP; black: passive membrane; red: active membrane contributes to the LFP).

(B) PSD frequency scaling for the control input simulation (line: mean PSD of seven recordings from L4 and L5; see Figure 2; shaded line: SEM). Broken horizontal lines indicate slopes of α = 2, 3, and 4. The vertical broken line indicates f = 40 Hz.

(C) PSD frequency scaling exponent α as a function of network state (top, fit for < 40 Hz; bottom, 40–1,000 Hz; circle: mean; error bar: SD). Quality-of-fit was assessed via the normalized root-mean-square error and linear correlation and was good for all cases (Table S2) so that α-values accurately depict power-scaling in the designated frequency bandwidths.

(D) V_e recordings from an individual L5 pyramid at three locations within L5 (voltage traces are clipped).

(E) PSD frequency scaling of individual L5 pyramidal neuron V_e contribution (bandwidth: 25–1,000 Hz; line: mean; shaded area: SEM; broken lines show slopes of 2, 3, and 4) for the three locations shown in (D).

(F) The value of frequency scaling exponent β indicates the frequency scaling of L5 pyramidal neurons at the single-neuron level as a function of network state (circle: mean; error bar: SD; lines of the same color report β in the three locations).

(G) V_e signal originating from a single L5 pyramidal neuron (same as in the middle of D) filtered at (top to bottom) <50 Hz, 50–100 Hz, and high pass (>800 Hz).

(H) The PSD of the filtered V_e traces are shown as a function of distance of the recording electrode from each L5 pyramidal neuron (line: mean; shaded area: SEM). For passive membranes, PSD scales differently as a function of distance for distances larger versus smaller than 100 µm. Broken lines indicate slopes γ = 2, 3, and 4.

(I) Distance scaling exponent γ denoting distance scaling of the V_e contribution of L5 pyramidal neurons at the single-neuron level as a function of network state (circle: mean of the three bandwidths; error bar: SD) for distances larger (top) or smaller (bottom) than 100 µm.

See also Tables S3 and S4.

membrane but also by the radically altered spatial constellation of extracellular sinks and sources. In agreement with recent work (Lindén et al., 2011; Pettersen et al., 2008; Schomburg et al., 2012), we find that the LFP length scale depends on the temporal coordination of the oscillatory inputs. Importantly, spiking and spike-related currents impact the LFP not only in the higher bandwidths but also in lower ones (<50 Hz) traditionally thought to reflect purely postsynaptic activity.

We found that L4 pyramids impacted the LFP and CSD within both layers, with their extracellular contribution greatly affected

by the presence or absence of active membranes. Conversely, L5 pyramids with their large somata, thick apical dendrites, and strong synaptic input contribute not only to the LFP within L5 but also to the LFP in L4, especially at the onset of coordinated synaptic input. Given their large size and powerful synaptic input, it is conceivable that L5 pyramids could also contribute to the LFP in other layers, such as L2/3 or L6, not simulated here. Thus, whereas the LFP reflects processing of neurons whose cell bodies are situated within that layer, the extended nature of pyramidal neurons gives rise to multipoles that reach into nearby layers. Importantly, we found this to be broadly true in simulations exhibiting varying degrees of input correlation.

In agreement with others (Pettersen et al., 2008; Schomburg et al., 2012), we find that L4/5 basket cells with their fairly low density (compared to excitatory neurons), localized and symmetric dendritic arbor, spatially uniform synaptic input, the small temporal width of their somatic spikes, and lack of strong afterpotentials have only a small impact on the LFP and CSD, even though their spike frequency is substantially higher than that of their excitatory neighbors (Figure 3C). Of course, this does not suggest that extracellular action potentials from individual basket cells are small.

When considering LFP characteristics, such as amplitude and spatiotemporal width, we observed that these are markedly shaped by the impinging pattern of postsynaptic currents and membrane characteristics. Increasing model complexity from only postsynaptic to using fully reconstructed active neurons attenuates the LFP amplitude, alters its spatiotemporal width and changes the sink-source location. Additionally, our findings regarding the LFP length scale (depending on input correlation, approximately 200–600 μm along the cortical depth and 100–300 μm tangentially) points to the necessity of large-scale models to study the origin and functionality of the LFP.

How do these observations compare with LFPs recorded during whisker stimulation (Riera et al., 2012)? Such stimulation triggers prominent thalamocortical input into L4 in somatosensory cortex (Brecht and Sakmann, 2002). At UP onset, and during the first 10–20 ms, the sink-source constellation in L4 and L5 was similar to experiments. Following the onset of synaptic depression in L5, the CSD became markedly different for the next 10–20 ms, with sink-source constellation inverting. Finally, after equilibration of synaptic weights in L4, the simulated CSD became almost identical to experiments. Given that the synaptic activation in our network was not designed to emulate whisker stimulation, we are led to the conclusion that while network computation requires inclusion of synaptic, morphological, and membrane characteristics, connectivity patterns, and features of synaptic dynamics, such as plasticity rules, are crucial not only for network processing but also to fully account for extracellular sinks and sources.

Sodium and potassium currents prominently contribute to the LFP in both layers with K currents dominating (approx. 40%–60%) the LFP during the UP-DOWN cycle. Although fast Na currents of local neurons contribute less than K ones, their contribution to the LFP is greater (approx. 10%–20%) than that of postsynaptic currents (<10% in most cases). Thus, it is true that synaptic input is reflected in the LFP in that it initiates and sustains the intracellular and membrane currents along neurons, but our simulations show that the LFP signal does not directly reflect synaptic activity. Instead, it predominantly reflects active membrane conductances activated by impinging postsynaptic input.

This observation challenges the classic view that LFPs are primarily a reflection of synaptic currents based on the number of activated synapses within a volume of brain tissue being typically much larger than the number of spikes (per unit time) within the same volume. Why do our simulations show such strong contribution of active membrane currents? The main reason is that during an individual spike, charge fluxes across the neural membrane at the perisomatic region (axon initial segment, soma, etc.) are much stronger than individual PSCs (Koch, 1999). While the strongest charge fluxes occur within 1–2 ms of every spike (according to the standard Hodgkin-Huxley model), a cascade of slower spiking currents (mainly K- but also Ca-dependent) with much longer time scales is coactivated. These slower active membrane conductances crucially contribute to the LFP as observed in Figure 7. On the other hand, fast synaptic currents (AMPA- and $GABA_A$-type) die out rapidly, while the slower ones (NMDA-type) have a fairly small contribution (the AMPA versus NMDA component of every excitatory synapse is about 1 to 0.7; Ramaswamy et al., 2012). (Notably, not all presynaptic inputs give rise to PSCs; Markram, 1997; Ramaswamy et al., 2012.) Finally, active conductances contribute much more to the LFP than passive ones because they are mainly located in the perisomatic region along large compartments (i.e., low axial resistance), such as the soma and near dendrites (especially for L5 pyramidal neurons), so that the associated return currents are spread along the whole morphology of the neuron. As a consequence, EAP amplitude is approximately proportional to the sum of the dendritic cross-sectional areas of all dendritic branches connected to the soma. Therefore, neurons with thick dendrites connected to the soma produce large EAPs and have the largest "radius of visibility" (Pettersen and Einevoll, 2008). At the same time, PSCs are mainly located along thin dendrites (i.e., much higher axial resistance), preventing return currents from spreading along the whole neural morphology.

Another important observation stemming from our simulations is the input specificity of the LFP composition. Although the LFP during the first 50–80 ms from UP onset is dominated by K currents originating from L5 pyramids for temporally coordinated input (Figure 7B), this switches to K currents from L4 pyramids for uncorrelated input (Figure 7A). Moreover, basket cells generally do not contribute markedly to the LFP, but this changes briefly 50 to 70 ms after UP onset. Thus, the LFP composition is not static but time- and state-dependent and is crucially impacted by the impinging input and the sort of subthreshold and spiking activity it induces (especially proximally to the recording site).

What are the functional (computational) ramifications of these observations? Coherence between spiking and specific LFP bands has been used to infer the relationship between synaptic input (hitherto considered to be reflected in the LFP) and neural output (spiking) and thereby specific mechanisms of information processing within and across brain regions (Fries et al., 1997; Lee et al., 2005; Montgomery et al., 2008; O'Keefe and Recce, 1993; Rutishauser et al., 2010; Womelsdorf et al.,

2006). This raises the question of the extent to which the locally generated LFP (or particular bandwidths of it) represent actual synaptic input impinging on local neurons rather than spiking output (Buzsáki et al., 2012). For example, it was recently shown that spiking coherence to ripples during sharp waves in CA1 is partly attributed to spiking currents shaping the ripple signal (Belluscio et al., 2012; Schomburg et al., 2012).

Another question arises regarding how perturbing rhythmic LFP activity such as theta with tetanic stimulation at particular phases of theta induces potentiation or depression of synaptic strength (Hölscher et al., 1997; Hyman et al., 2003; Pavlides et al., 1988). Other studies relate cognitive alteration to perturbation of neocortical UP-DOWN states (Marshall et al., 2006) or hippocampal sharp waves (Girardeau et al., 2009). Our population model does not attempt to reproduce any particular LFP rhythm, but it does link the LFP to biophysical processing. Thus, it can become a useful tool toward addressing the involvement of particular mechanisms during particular LFP bandwidths and phases and how perturbing them crucially alters other processing and, ultimately, cognitive function.

When modeling the impact of active membranes on LFP power scaling, we found an inverse power law (Miller et al., 2009; Milstein et al., 2009) with scaling exponent α depending on input correlation and bandwidth of interest. Passive membrane consistently resulted in larger exponents for higher bandwidths (40–1,000 Hz). When zooming in to the level of individual L5 pyramids by calculating the scaling exponent β, active membrane contributions differ substantially from passive membrane ones not just for higher bandwidths but, importantly, down to low frequencies (<50 Hz). Interestingly, β compares much better to α in the 40–1,000 Hz range than below 40 Hz for synaptic only and passive membranes. Yet, in the presence of active membrane conductances, β becomes comparable to α, both in the lower and higher bandwidth (especially so for the control and supersynchronized scenarios), suggesting very similar scaling between the entire population and L5 pyramidal neurons, regardless of their exact location within L5.

We also looked at PSD distance scaling (exponent γ)—within a 100 μm radius, PSD scales with $\gamma \approx 2$, characteristic of a dipole. For larger distances, $\gamma \approx 3$. A recent study elegantly illustrated that as long as $\gamma > 2$, the contribution of successive more distant populations of neurons to the LFP saturates, that is, the LFP has a finite spatial reach (Lindén et al., 2011). In our simulations, for active membranes, PSD consistently scales with distance as $\gamma \approx 3$. To generalize, for smaller distances, postsynaptic currents contribute as monopoles ($\gamma \approx 1$), the presence of passive membranes gives rise to return currents and an additional pole ($\gamma \approx 2$), and active conductances give rise to leakier membranes, resulting in a third pole ($\gamma \approx 3$). For larger distances, power scaling of active and passive membranes is similar ($\gamma \approx 3$). Concurrently, an increase in input correlation results in an increase in LFP amplitude and, importantly, length scale. Thus, whereas the LFP is a good estimator of local neural processing, the volume it is representative for (within the same layer) can change substantially.

The present biophysical model does not include glial and astrocytic processes likely to be important for slowly fluctuating components of the LFP and we do not include nonmyelinated presynaptic axonal compartments (though Gold et al., 2006; Schomburg et al., 2012; and our own modeling indicate they contribute minimally to the LFP). Likewise, we neglected contributions of presynaptic terminals; given their small size, it is likely that the associated local return currents will render their contribution nugatory. Diffusion was also excluded in our simulations, which can lead to 1/f-scaling (Bédard and Destexhe, 2009). Finally, in our simulations we assumed a purely resistive and homogeneous extracellular medium. There is evidence in favor of a purely ohmic extracellular medium for frequencies <500 Hz, but at least one study has emphasized a capacitive component (Bédard et al., 2004), which, if true, may alter some of the findings in terms of the LFP contributions of all processes involved. Moreover, even for the purely resistive case, conductivity experiments have shown that the extracellular medium is inhomogeneous, i.e., resistivity gradients exist (Goto et al., 2010). Although the model can be extended to account for such observations, our primary goal is to account for the conventional biophysical processes related to LFP generation and the impact of active membrane conductances in particular.

Despite these limitations, our model reproduces a number of observations. First, external synaptic input gives rise to spike frequencies compatible with in vivo observations during slow-wave activity. The simulated EAP waveforms from our pyramids and basket cells agree with experimental observations (Gold et al., 2006). Our simulations suggest the LFP contribution of fast spiking basket cells is small, as also shown in Lindén et al. (2011) and Schomburg et al. (2012). Furthermore, our active simulations generate LFPs and CSDs that agree, both in terms of spatial constellation (Riera et al., 2012) and spectral content (Miller et al., 2009; Milstein et al., 2009), with in vivo observations, especially after UP onset. Using passive morphologies, we were able to reproduce the observation that LFP power scales differently within versus outside a 100 μm radius from the recording electrode (Lindén et al., 2011). This changed substantially in the presence of active membranes. Finally, increasing input correlation resulted in larger LFP amplitudes and length scales, both for active and passive membranes. Richard Feynman once famously wrote: "what I cannot create, I do not understand." It is our belief that the present approach is a necessary step toward unraveling the biophysics of LFPs and the workings of brain circuitry, in general.

EXPERIMENTAL PROCEDURES

The Core Simulation

The model and simulations were developed using the software and hardware infrastructure of the Blue Brain Facility, including data, models, and workflows for modeling rat (P12–P16) cortical S1 microcircuitry. Network simulations were performed using NEURON software (Hines and Carnevale, 1997) running on a Blue Gene P supercomputer on 1,024 nodes and 4,096 CPUs. Four seconds of simulated time took approx. 3 hr to compute. A collection of tools and templates written in HOC and NMODL were employed to handle the setup and configuration on the parallel machine architecture (Hines et al., 2008).

Electrophysiology and Morphological Reconstruction

Electrophysiology and reconstruction protocols are described in Hay et al. (2011). Briefly, the firing response was obtained from slice whole-cell patch-clamp recordings in rat S1. For L4 and L5 pyramidal neurons, protocols were identical to Hay et al. (2011). For the basket cells, we used some

additional stimulation protocols (Toledo-Rodriguez et al., 2004). After the experiment, brain slices were fixed and incubated overnight. Morphological reconstruction was performed from well-stained neurons exhibiting only few cut neurite branches.

Computational Reconstruction of Neurons

Single-neuron computational modeling is described in Hay et al. (2011). Briefly, neurons were represented as a compartmental, conductance-based model using reconstructed morphologies from rat S1. The compartments were separated in four zones: axon initial segment (AIS), soma, basal dendrites, and apical dendrites (Figure 1). The full axon was not simulated; only the AIS was simulated (Figure 1, bottom row). Synapses at the postsynaptic cells were activated after spike detection in AIS in the control case and prerecorded spike trains otherwise. A conduction delay based on axonal path distance to the soma (assuming spike conduction velocity was 300 μm/ms; Stuart et al., 1997) was accounted for. Passive membrane capacitance was 1 $\mu F/cm^2$ for the soma, AIS, and dendrites, whereas for pyramids it was 2 $\mu F/cm^2$ for basal and apical dendrites to correct for dendritic spine area. Axial resistance was 100 Ω cm for all compartments. Input resistance R_{in} was 225 ± 41 MΩ for L4 pyramids and 74 ± 35 MΩ for L5 pyramids. For basket cells, R_{in} = 379 ± 210 MΩ. The resting potential was −74.1 ± 0.1 mV for L4 pyramids, −73.8 ± 0.1 mV for L5 pyramids, and −71.6 ± 1.4 mV for basket cells.

Up to ten active membrane conductance types were accounted for with kinetics taken from the published ion channel models or from published experimental data (Hay et al., 2011). The reversal potentials for sodium and potassium were 50 and −85 mV, respectively, and −45 mV was used for the I_h current. Ion currents were modeled using the Hodgkin-Huxley formalism.

Network Connectivity

Connectivity patterns were implemented as presented in Hill et al. (2012). Briefly, reconstructed cells from L4 and L5 were placed in a hexagonal volume with a radius of 320 μm, matching biological densities of approx. 240,000 per mm^3 in L4 and 90,000 per mm^3 in L5 (J. Gonzalez-Soriano, J. DeFelipe, L. Alonso-Nanclares, personal communication). Every axonal part closer than 3 μm to a dendrite is detected, and synapses are placed at a 5% subset of these appositions. The subset is chosen such that the number of synapses per connection and synaptic bouton densities match biological values. Spatial distributions of synapses placed in such manner are known to match biological distribution for a number of intracortical pathways with a mean error <8%.

Synaptic Dynamics

All 15,137,757 synapses were modeled using conductance changes. AMPA- and NMDA-type synapses accounted for excitation. For AMPA receptor (AMPAR) kinetics, the synaptic conductance was 0.3 ± 0.2 nS. The rise and decay time constants were 0.2 ± 0.05 ms and 1.7 ± 0.18 ms, respectively. For NMDAR kinetics, conductance was 0.2 ± 0.1 nS with rise and decay times, 0.29 ± 0.23 ms and 43 ± 1.2 ms, respectively. The reversal potential of AMPAR and NMDAR was 0 mV. For inhibitory $GABA_A$ synapses, the mean conductance was 0.66 ± 0.2 nS with the rise and decay time constants, 0.2 ± 0.05 ms and 8.3 ± 2.2 ms. Time constant for recovery from depression and time constant for recovery from facilitation were adopted (Angulo et al., 1999; Gupta et al., 2000) and assigned to each putative inhibitory synaptic location identified by the collision-detection algorithm. The $GABA_A$ reversal was −80 mV. External input is mediated by distributing additional excitatory and inhibitory synapses randomly (uniform distribution) across all cells and activating them independently with a temporally modulated frequency. External synapses accounted for approximately 5% of the total number of synapses.

Spiking Synchrony

To measure spiking synchrony, we calculated the mean of the normalized joint peristimulus time (PST) histogram at a lag of 0 ms, i.e., the mean cross-covariance of PST histograms of cell pairs, normalized by the product of their SD. To generate the histograms, we used a bin width of 1 ms. As the covariance would be affected by the change in firing rates between simulated UP and DOWN, we limited the analysis to spikes elicited during UP. To remove synchrony from the simulation (uncorrelated case), we first generated artificial spike trains by moving all spikes of the control case to times randomly chosen between 0 and 4,000 ms. This generated independent stationary Poisson spike trains with the same number of spikes as in the control case. This spike train was then used to drive synapses in a simulation. The external input was also present but with a constant rate equal to the mean of the rate in the control case. To increase synchrony (supersynchronized case), we moved all spike times of the control case to the nearest multiple of 5 ms. External input in this case was identical to the control case.

Extracellular Field Calculation

The extracellular contribution of transmembrane currents of all neural compartments (approx. 410 compartments per cell, >5,000,000 in total) was calculated via the line source approximation, LSA (Holt and Koch, 1999). Briefly, assuming a purely homogeneous and resistive (3.5 Ω m) extracellular medium, Laplace's equation applies $\nabla^2 V_e = 0$. At the boundaries, $(1/\rho)V_e = J_m$ with ρ being the resistivity and J_m the transmembrane current density. LSA assumes each cylindrical compartment of the spatially discretized neuron as a line (a cylinder of infinitesimally small diameter) with a constant current density along the line. The V_e contributed by current I_j of each neural compartment j evenly distributed over the line segment of length Δs_j and the overall extracellular voltage $V_e(\vec{r},t)$ becomes

$$V_e(\vec{r},t) = \sum_{j=1}^{N} \frac{\rho I_j(t)}{4\pi\Delta s_j} \log \frac{\sqrt{h_j^2 + r_j^2} - h_j}{\sqrt{l_j^2 + r_j^2} - l_j},$$

with r_j being the radial distance from line segment, h_j the longitudinal distance from the end of the line segment, and $l_j = \Delta s_j + h_j$ the distance from the start of the line segment. The LSA was found to be accurate, except at very small distances (a few micrometers) from the cable.

Calculation of V_e using the LSA took place on a separate computer cluster (SGI) and took approx. 1 hr. The CSD was estimated as the negative second spatial derivative along the depth axis. We also calculated the CSD via iCSD (Łęski et al., 2011), and the outcome remained very similar. We thus used the conventional CSD definition.

SUPPLEMENTAL INFORMATION

Supplemental Information includes four tables and four figures and can be found with this article online at http://dx.doi.org/10.1016/j.neuron.2013.05.023.

ACKNOWLEDGMENTS

This work was supported by the National Institute of Neurological Disorders and Stroke, Human Frontier Science Program, Swiss National Science Foundation, the Allen Institute for Brain Science, and the Mathers Charitable Foundation and by funding to the Blue Brain Project by the ETH Board and EPFL. Financial support for the CADMOS Blue Gene/P system was provided by the Canton of Geneva, Canton of Vaud, Hans Wilsdorf Foundation, Louis-Jeantet Foundation, University of Geneva, University of Lausanne, and EPFL. Special thanks goes to G. Buzsáki, E. Schomburg, A. Shai, Y. Billeh, J. Taxidis, and members of the Blue Brain Consortium, in particular, Michael Hines, James King, Eilif Muller, Srikant Ramaswamy, Felix Schürmann, and Werner van Geit.

Accepted: May 16, 2013
Published: July 24, 2013

REFERENCES

Achermann, P., and Borbély, A.A. (1997). Low-frequency (< 1 Hz) oscillations in the human sleep electroencephalogram. Neuroscience *81*, 213–222.

Anastassiou, C.A., Montgomery, S.M., Barahona, M., Buzsáki, G., and Koch, C. (2010). The effect of spatially inhomogeneous extracellular electric fields on neurons. J. Neurosci. *30*, 1925–1936.

Anastassiou, C.A., Perin, R., Markram, H., and Koch, C. (2011). Ephaptic coupling of cortical neurons. Nat. Neurosci. *14*, 217–223.

Angulo, M.C., Rossier, J., and Audinat, E. (1999). Postsynaptic glutamate receptors and integrative properties of fast-spiking interneurons in the rat neocortex. J. Neurophysiol. *82*, 1295–1302.

Bédard, C., and Destexhe, A. (2009). Macroscopic models of local field potentials and the apparent 1/f noise in brain activity. Biophys. J. *96*, 2589–2603.

Bédard, C., Kröger, H., and Destexhe, A. (2004). Modeling extracellular field potentials and the frequency-filtering properties of extracellular space. Biophys. J. *86*, 1829–1842.

Bédard, C., Kröger, H., and Destexhe, A. (2006). Does the 1/f frequency scaling of brain signals reflect self-organized critical states? Phys. Rev. Lett. *97*, 118102.

Belluscio, M.A., Mizuseki, K., Schmidt, R., Kempter, R., and Buzsáki, G. (2012). Cross-frequency phase-phase coupling between θ and γ oscillations in the hippocampus. J. Neurosci. *32*, 423–435.

Brecht, M., and Sakmann, B. (2002). Dynamic representation of whisker deflection by synaptic potentials in spiny stellate and pyramidal cells in the barrels and septa of layer 4 rat somatosensory cortex. J. Physiol. *543*, 49–70.

Buzsáki, G. (2004). Large-scale recording of neuronal ensembles. Nat. Neurosci. *7*, 446–451.

Buzsaki, G., and Traub, R. (1996). Physiological basis of EEG activity. In Epilepsy, a Comprehensive Textbook, J. Engel, Jr. and T.A. Pedley, eds. (New York: Raven Press).

Buzsáki, G., Anastassiou, C.A., and Koch, C. (2012). The origin of extracellular fields and currents—EEG, ECoG, LFP and spikes. Nat. Rev. Neurosci. *13*, 407–420.

Buzsaki, G., Bickford, R.G., Ponomareff, G., Thal, L.J., Mandel, R., and Gage, F.H. (1988). Nucleus basalis and thalamic control of neocortical activity in the freely moving rat. J. Neurosci. *8*, 4007–4026.

Chrobak, J.J., Lörincz, A., and Buzsáki, G. (2000). Physiological patterns in the hippocampo-entorhinal cortex system. Hippocampus *10*, 457–465.

Druckmann, S., Banitt, Y., Gidon, A., Schürmann, F., Markram, H., and Segev, I. (2007). A novel multiple objective optimization framework for constraining conductance-based neuron models by experimental data. Front. Neurosci. *1*, 7–18.

Elul, R. (1971). The genesis of the EEG. Int. Rev. Neurobiol. *15*, 227–272.

Fanselow, E.E., and Connors, B.W. (2010). The roles of somatostatin-expressing (GIN) and fast-spiking inhibitory interneurons in UP-DOWN states of mouse neocortex. J. Neurophysiol. *104*, 596–606.

Fries, P., Roelfsema, P.R., Engel, A.K., König, P., and Singer, W. (1997). Synchronization of oscillatory responses in visual cortex correlates with perception in interocular rivalry. Proc. Natl. Acad. Sci. USA *94*, 12699–12704.

Girardeau, G., Benchenane, K., Wiener, S.I., Buzsáki, G., and Zugaro, M.B. (2009). Selective suppression of hippocampal ripples impairs spatial memory. Nat. Neurosci. *12*, 1222–1223.

Gold, C., Henze, D.A., Koch, C., and Buzsáki, G. (2006). On the origin of the extracellular action potential waveform: A modeling study. J. Neurophysiol. *95*, 3113–3128.

Gold, C., Henze, D.A., and Koch, C. (2007). Using extracellular action potential recordings to constrain compartmental models. J. Comput. Neurosci. *23*, 39–58.

Goto, T., Hatanaka, R., Ogawa, T., Sumiyoshi, A., Riera, J., and Kawashima, R. (2010). An evaluation of the conductivity profile in the somatosensory barrel cortex of Wistar rats. J. Neurophysiol. *104*, 3388–3412.

Gupta, A., Wang, Y., and Markram, H. (2000). Organizing principles for a diversity of GABAergic interneurons and synapses in the neocortex. Science *287*, 273–278.

Haider, B., Duque, A., Hasenstaub, A.R., and McCormick, D.A. (2006). Neocortical network activity in vivo is generated through a dynamic balance of excitation and inhibition. J. Neurosci. *26*, 4535–4545.

Hay, E., Hill, S., Schürmann, F., Markram, H., and Segev, I. (2011). Models of neocortical layer 5b pyramidal cells capturing a wide range of dendritic and perisomatic active properties. PLoS Comput. Biol. *7*, e1002107.

Hill, S.L., Wang, Y., Riachi, I., Schürmann, F., and Markram, H. (2012). Statistical connectivity provides a sufficient foundation for specific functional connectivity in neocortical neural microcircuits. Proc. Natl. Acad. Sci. USA *109*, E2885–E2894.

Hines, M.L., and Carnevale, N.T. (1997). The NEURON simulation environment. Neural Comput. *9*, 1179–1209.

Hines, M.L., Markram, H., and Schürmann, F. (2008). Fully implicit parallel simulation of single neurons. J. Comput. Neurosci. *25*, 439–448.

Hölscher, C., Anwyl, R., and Rowan, M.J. (1997). Stimulation on the positive phase of hippocampal theta rhythm induces long-term potentiation that can Be depotentiated by stimulation on the negative phase in area CA1 in vivo. J. Neurosci. *17*, 6470–6477.

Holt, G.R., and Koch, C. (1999). Electrical interactions via the extracellular potential near cell bodies. J. Comput. Neurosci. *6*, 169–184.

Hyman, J.M., Wyble, B.P., Goyal, V., Rossi, C.A., and Hasselmo, M.E. (2003). Stimulation in hippocampal region CA1 in behaving rats yields long-term potentiation when delivered to the peak of theta and long-term depression when delivered to the trough. J. Neurosci. *23*, 11725–11731.

Jefferys, J.G. (1995). Nonsynaptic modulation of neuronal activity in the brain: electric currents and extracellular ions. Physiol. Rev. *75*, 689–723.

Jefferys, J.G.R., and Haas, H.L. (1982). Synchronized bursting of CA1 hippocampal pyramidal cells in the absence of synaptic transmission. Nature *300*, 448–450.

Katzner, S., Nauhaus, I., Benucci, A., Bonin, V., Ringach, D.L., and Carandini, M. (2009). Local origin of field potentials in visual cortex. Neuron *61*, 35–41.

Koch, C. (1999). Biophysics of Computation: Information Processing in Single Neurons (Oxford, England: Oxford University Press).

Lee, H., Simpson, G.V., Logothetis, N.K., and Rainer, G. (2005). Phase locking of single neuron activity to theta oscillations during working memory in monkey extrastriate visual cortex. Neuron *45*, 147–156.

Łęski, S., Pettersen, K.H., Tunstall, B., Einevoll, G.T., Gigg, J., and Wójcik, D.K. (2011). Inverse current source density method in two dimensions: inferring neural activation from multielectrode recordings. Neuroinformatics *9*, 401–425.

Lindén, H., Tetzlaff, T., Potjans, T.C., Pettersen, K.H., Grün, S., Diesmann, M., and Einevoll, G.T. (2011). Modeling the spatial reach of the LFP. Neuron *72*, 859–872.

Logothetis, N.K., and Wandell, B.A. (2004). Interpreting the BOLD signal. Annu. Rev. Physiol. *66*, 735–769.

Logothetis, N.K., Kayser, C., and Oeltermann, A. (2007). In vivo measurement of cortical impedance spectrum in monkeys: implications for signal propagation. Neuron *55*, 809–823.

Luczak, A., Barthó, P., Marguet, S.L., Buzsáki, G., and Harris, K.D. (2007). Sequential structure of neocortical spontaneous activity in vivo. Proc. Natl. Acad. Sci. USA *104*, 347–352.

Luczak, A., Barthó, P., and Harris, K.D. (2009). Spontaneous events outline the realm of possible sensory responses in neocortical populations. Neuron *62*, 413–425.

Markram, H. (1997). A network of tufted layer 5 pyramidal neurons. Cereb. Cortex *7*, 523–533.

Marshall, L., Helgadóttir, H., Mölle, M., and Born, J. (2006). Boosting slow oscillations during sleep potentiates memory. Nature *444*, 610–613.

Miller, K.J., Sorensen, L.B., Ojemann, J.G., and den Nijs, M. (2009). Power-law scaling in the brain surface electric potential. PLoS Comput. Biol. *5*, e1000609.

Milstein, J., Mormann, F., Fried, I., and Koch, C. (2009). Neuronal shot noise and Brownian 1/f2 behavior in the local field potential. PLoS ONE *4*, e4338.

Mitzdorf, U. (1985). Current source-density method and application in cat cerebral cortex: investigation of evoked potentials and EEG phenomena. Physiol. Rev. *65*, 37–100.

Montgomery, S.M., Sirota, A., and Buzsáki, G. (2008). Theta and gamma coordination of hippocampal networks during waking and rapid eye movement sleep. J. Neurosci. *28*, 6731–6741.

Mukovski, M., Chauvette, S., Timofeev, I., and Volgushev, M. (2007). Detection of active and silent states in neocortical neurons from the field potential signal during slow-wave sleep. Cereb. Cortex *17*, 400–414.

Nicholson, C., and Freeman, J.A. (1975). Theory of current source-density analysis and determination of conductivity tensor for anuran cerebellum. J. Neurophysiol. *38*, 356–368.

Nunez, P.L., and Srinivasan, R. (2006). Electric Fields of the Brain (New York: Oxford University Press, USA).

O'Keefe, J., and Recce, M.L. (1993). Phase relationship between hippocampal place units and the EEG theta rhythm. Hippocampus *3*, 317–330.

Oberlaender, M., de Kock, C.P.J., Bruno, R.M., Ramirez, A., Meyer, H.S., Dercksen, V.J., Helmstaedter, M., and Sakmann, B. (2012). Cell type-specific three-dimensional structure of thalamocortical circuits in a column of rat vibrissal cortex. Cereb. Cortex *22*, 2375–2391.

Pavlides, C., Greenstein, Y.J., Grudman, M., and Winson, J. (1988). Long-term potentiation in the dentate gyrus is induced preferentially on the positive phase of theta-rhythm. Brain Res. *439*, 383–387.

Perin, R., Berger, T.K., and Markram, H. (2011). A synaptic organizing principle for cortical neuronal groups. Proc. Natl. Acad. Sci. USA *108*, 5419–5424.

Pettersen, K.H., and Einevoll, G.T. (2008). Amplitude variability and extracellular low-pass filtering of neuronal spikes. Biophys. J. *94*, 784–802.

Pettersen, K.H., Hagen, E., and Einevoll, G.T. (2008). Estimation of population firing rates and current source densities from laminar electrode recordings. J. Comput. Neurosci. *24*, 291–313.

Pritchard, W.S. (1992). The brain in fractal time: 1/f-like power spectrum scaling of the human electroencephalogram. Int. J. Neurosci. *66*, 119–129.

Ramaswamy, S., Hill, S.L., King, J.G., Schürmann, F., Wang, Y., and Markram, H. (2012). Intrinsic morphological diversity of thick-tufted layer 5 pyramidal neurons ensures robust and invariant properties of in silico synaptic connections. J. Physiol. *590*, 737–752.

Rasch, M., Logothetis, N.K., and Kreiman, G. (2009). From neurons to circuits: linear estimation of local field potentials. J. Neurosci. *29*, 13785–13796.

Ray, S., and Maunsell, J.H.R. (2011). Different origins of gamma rhythm and high-gamma activity in macaque visual cortex. PLoS Biol. *9*, e1000610.

Riera, J.J., Ogawa, T., Goto, T., Sumiyoshi, A., Nonaka, H., Evans, A., Miyakawa, H., and Kawashima, R. (2012). Pitfalls in the dipolar model for the neocortical EEG sources. J. Neurophysiol. *108*, 956–975.

Rutishauser, U., Ross, I.B., Mamelak, A.N., and Schuman, E.M. (2010). Human memory strength is predicted by theta-frequency phase-locking of single neurons. Nature *464*, 903–907.

Sanchez-Vives, M.V., and McCormick, D.A. (2000). Cellular and network mechanisms of rhythmic recurrent activity in neocortex. Nat. Neurosci. *3*, 1027–1034.

Schomburg, E.W., Anastassiou, C.A., Buzsáki, G., and Koch, C. (2012). The spiking component of oscillatory extracellular potentials in the rat hippocampus. J. Neurosci. *32*, 11798–11811.

Steriade, M., Nuñez, A., and Amzica, F. (1993a). A novel slow (< 1 Hz) oscillation of neocortical neurons in vivo: depolarizing and hyperpolarizing components. J. Neurosci. *13*, 3252–3265.

Steriade, M., Contreras, D., Curró Dossi, R., and Nuñez, A. (1993b). The slow (< 1 Hz) oscillation in reticular thalamic and thalamocortical neurons: scenario of sleep rhythm generation in interacting thalamic and neocortical networks. J. Neurosci. *13*, 3284–3299.

Steriade, M., Nuñez, A., and Amzica, F. (1993c). Intracellular analysis of relations between the slow (< 1 Hz) neocortical oscillation and other sleep rhythms of the electroencephalogram. J. Neurosci. *13*, 3266–3283.

Stuart, G., Schiller, J., and Sakmann, B. (1997). Action potential initiation and propagation in rat neocortical pyramidal neurons. J. Physiol. *505*, 617–632.

Toledo-Rodriguez, M., Blumenfeld, B., Wu, C., Luo, J., Attali, B., Goodman, P., and Markram, H. (2004). Correlation maps allow neuronal electrical properties to be predicted from single-cell gene expression profiles in rat neocortex. Cereb. Cortex *14*, 1310–1327.

Womelsdorf, T., Fries, P., Mitra, P.P., and Desimone, R. (2006). Gamma-band synchronization in visual cortex predicts speed of change detection. Nature *439*, 733–736.